

Enhancing the vision-language foundation model with key semantic knowledge-emphasized report refinement

Cheng Li^{a,1}, Weijian Huang^{a,b,c,1}, Hao Yang^{a,b,c}, Jiarun Liu^{a,b,c}, Shanshan Wang^{a,c,*}

^aPaul C. Lauterbur Research Center for Biomedical Imaging, Shenzhen Institute of Advanced Technology, Chinese Academy of Sciences, Shenzhen 518055, China

^bUniversity of Chinese Academy of Sciences, Beijing 100049, China

^cPeng Cheng Laboratory, Shenzhen 518066, China

1. These authors contributed equally to this work.

* Corresponding author: Shanshan Wang (ss.wang@siat.ac.cn)

Abstract

Recently, vision-language representation learning has made remarkable advancements in building up medical foundation models, holding immense potential for transforming the landscape of clinical research and medical care. The underlying hypothesis is that the rich knowledge embedded in radiology reports can effectively assist and guide the learning process, reducing the need for additional labels. However, these reports tend to be complex and sometimes even consist of redundant descriptions that make the representation learning too challenging to capture the key semantic information. This paper develops a novel iterative vision-language representation learning framework by proposing a key semantic knowledge-emphasized report refinement method. Particularly, raw radiology reports are refined to highlight the key information according to a constructed clinical dictionary and two model-optimized knowledge-enhancement metrics. The iterative framework is designed to progressively learn, starting from gaining a general understanding of the patient's condition based on raw reports and gradually refines and extracts critical information essential to the fine-grained analysis tasks. The effectiveness of the proposed framework is validated on various downstream medical image analysis tasks, including disease classification, region-of-interest segmentation, and phrase grounding. Our framework surpasses seven state-of-the-art methods in both fine-tuning and zero-shot settings, demonstrating its encouraging potential for different clinical applications.

Keywords:

Vision-language representation learning, Medical foundation models, Knowledge-emphasized report refinement, Iterative learning

1. Introduction

In modern clinical practice, medical imaging plays a crucial role in the detection, monitoring of progression, and evaluation of treatment prognosis for various diseases [1]–[3]. However, the exponential growth of imaging data poses a significant burden to radiologists, impacting the efficiency of clinical workflows. To tackle this issue, artificial intelligence, particularly deep learning, has emerged as a revolutionary technique, automating medical image analysis and aiding in clinical decision-making [4]–[7]. Nevertheless, manually annotating large datasets necessary to train respective deep learning models for each task is time-consuming and requires the expertise of domain specialists [8], [9]. As a result, there is an urgent need to develop effective medical foundation models that can handle various downstream tasks without relying on collecting large-scale labeled datasets [10], [11].

One promising and natural solution is to leverage the valuable information embedded within radiology reports [11], which are routinely collected in clinical practice. These reports contain rich domain knowledge that can effectively assist and guide image representation learning, thereby reducing the need for costly manual labels. A straightforward method in this direction involves extracting supervision signals directly from the reports. Various techniques, such as natural language processing (NLP) techniques and rule-based labelers, have been proposed for this purpose [12], [13]. However, these labeling techniques often rely on fixed lexicons and manually engineered rules, making it difficult to adapt them to new scenarios. Another successful avenue is the application of implicit supervision through vision-language representation learning, which has demonstrated great success in natural image recognition tasks [14]–[16]. Nevertheless, the transfer of this technique to the medical domain faces many challenges [17]. One of the major obstacles is the presence of complex and sometimes redundant medical entity descriptions within radiology reports, which can pose significant difficulties for effective representation learning [18], [19].

In this study, our primary objective is to enhance the medical vision-language foundation model by proposing a key semantic knowledge-emphasized report refinement method. Incorporating the proposed report refinement method, we develop a novel iterative vision-language representation learning framework. On the one hand, to refine the reports, we construct a simple yet effective clinical dictionary to link keywords in raw radiology reports with medical knowledge-supplemented sentences. Then, two model-optimized knowledge-enhancement metrics are constructed to guide the report refinement process using the medical knowledge-supplemented sentences such that the key information relevant to fine-grained downstream analysis tasks is effectively highlighted. On the other hand, our iterative framework enables the model to progressively learn the intricate medical information contained in radiology reports (Fig. 1). In the first iteration, we utilize the raw radiology reports as the initial source of information to gain a general understanding of the patient's condition, as provided by the radiologists. This step serves as a preliminary knowledge extraction process,

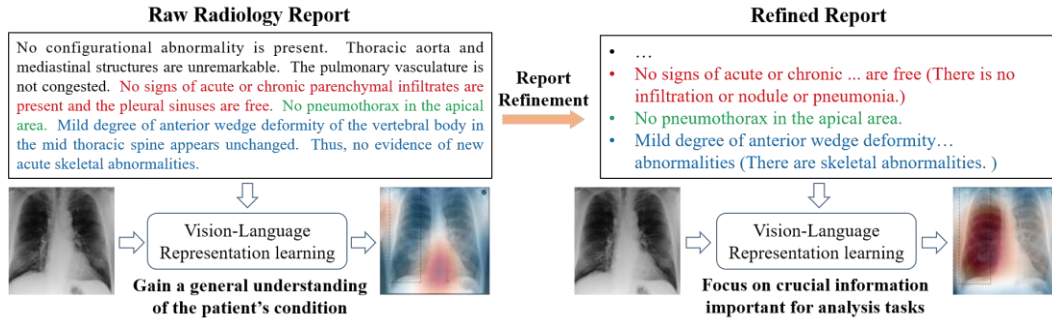


Figure 1. Our proposed iterative vision-language representation learning framework. In the first iteration, the raw radiology reports are leveraged to gain a general understanding of the patient's condition. In the second stage, the refined reports are employed to further fine-tune the model, guiding the model towards capturing crucial information.

obtaining the model to calculate the two model-optimized knowledge-enhancement metrics. In the second stage, we employ refined reports to further fine-tune the model, directing its attention towards crucial information. The effectiveness of the proposed framework is validated by extensive downstream medical image analysis experiments, including disease classification, region-of-interest segmentation, and phrase grounding. The results demonstrate that our framework surpasses state-of-the-art vision-language representation learning methods in both fine-tuning and zero-shot settings.

Our main contributions can be summarized as follows:

- We develop a novel iterative vision-language representation learning framework, which is designed to firstly gain a general understanding of the patient's condition from the raw radiology reports and then extract critical information by refining reports to capture the essential fine-grained features from the images.
- We propose a key semantic knowledge-emphasized report refinement method. Under the guidance of a specially constructed clinical dictionary and two model-optimized knowledge-enhancement metrics, the reports are refined to highlight crucial information essential to fine-grained downstream image analysis tasks.
- Extensive experimental validations were conducted on multiple external datasets, covering various medical image analysis tasks. The results demonstrate that our proposed framework outperforms recent state-of-the-art vision-language representation methods in both fine-tuning and zero-shot settings, showcasing its effectiveness and robustness.

2. Related Work

In this section, we provide a concise overview of recent research that focuses on utilizing information from radiology reports for medical image representation learning. We categorize these works into two main groups based on the strategies they employ:

those that use explicit supervision signals extracted from radiology reports and those that incorporate implicit supervision through multi-modal vision-language representation learning.

2.1 Report-supervised medical image representation learning

Utilizing explicit supervision signals extracted from radiology reports to supervise the learning of medical imaging models is an intuitive and straightforward approach, particularly in scenarios where manual labels are not readily available. Wang et al. demonstrated the feasibility of this approach by constructing a chest X-ray dataset (ChestX-ray8) at a hospital scale [12]. They employed NLP tools to search for the presence of 8 common thoracic pathology keywords in corresponding radiology reports and developed specific rules to remove negation and uncertainty. Then, they built a weakly supervised classification and localization framework using this dataset, validating the effectiveness of the automatically generated labels for these two important medical image analysis tasks. Another notable work in this area is by Irvin et al. [13], who developed a rule-based labeler to extract structured labels for images from free-text radiology reports. Their efforts resulted in the construction of the well-known dataset, CheXpert. Leveraging the extracted labels, they trained convolutional neural networks using different uncertainty approaches to classify 14 observations, and their best model achieved higher performance than 3 additional radiologists on detecting 3 out of 5 selected pathologies, cardiomegaly, edema, and pleural effusion, validating the effectiveness of the generated labels for the detection of common chest radiographic observations.

Despite the effectiveness of these report-based automatic labeling approaches on individual datasets and specific tasks, there are two main limitations that hinder their widespread adoption. One limitation is that the relevant labeling rules are manually crafted. This manual process can introduce inaccuracies, resulting in the generation of incorrect labels [17]. Moreover, these labeling rules are often designed to capture a limited set of clinical observations mentioned in the reports, which can potentially overlook important information contained within the reports [17]. Another limitation of the approach is that the labeling rules are domain- and style-specific, and they rely on fixed lexicons. Consequently, the effectiveness of the developed labeling techniques may not generalize well to new scenarios or different datasets [20].

2.2 Medical vision-language representation learning

Different from the approach of directly extracting supervision signals from radiology reports, medical vision-language representation learning leverages implicit supervision from the reports by simultaneously learning multi-modal representations. There are two main categories of methods in this area: those employing masked autoencoders [20], [21] and those employing contrastive learning techniques [17], [22]–[25]. Methods

using masked autoencoders aim to learn vision-language representations by restoring the original images and reports. For example, Chen et al. focuses on learning joint vision-language representations, which can be applied to various downstream tasks such as visual question answering, image-text classification, and image-caption retrieval [21]. Zhou et al. targets the learning of radiographic representations for disease diagnosis [20]. These methods based on masked autoencoders typically require fine-tuning for evaluation due to the discrepancy between the pre-text restoration task and the downstream medical image recognition tasks. They may lack zero-shot capability. Contrastive learning-based methods, on the other hand, learn vision-language representations by aligning the distributions of multi-modal features. These methods can be employed for medical image recognition tasks in both fine-tuning and zero-shot settings. Among these works, Zhang et al. introduced the pioneering framework ConVIRT [17], which learns medical image representations from paired images and reports by employing a bidirectional contrastive objective. Similarly, Tiu et al. proposed CheXzero, which achieved expert-level detection of pathologies without fine-tuning using labeled data [25]. To capture localized features and fine-grained semantics in medical images, Huang et al. proposed GLoRIA, a multimodal global-local representation learning framework [23]. Zhou et al. introduced REFERS, which performs report generation in addition to multi-modal contrastive learning to facilitate the learning of well-transferable image representations [24]. To simplify the training of medical vision-language representation models, Liu et al. proposed M-FLAG, which trains only the vision model while freezing the language model [22].

While medical vision-language representation learning has shown promising results, there are still challenges to overcome. One major obstacle is the presence of complex and sometimes even redundant medical entity descriptions within radiology reports. To address this issue, researchers have explored different approaches. For example, Boecking et al. trained a radiology-specific text encoder, called CXR-BERT, in their BioViL model to better handle radiology reports [26]. Additionally, Wu et al. and Zhang et al. proposed methods to simplify radiology reports by extracting medical-related information before inputting them into the text encoders [18], [19]. The primary objective of our study is to refine the radiology reports by emphasizing key semantic knowledge to enhance vision-language representation learning. Different from the approaches of Wu et al. and Zhang et al., which employ specific modules to extract medical entities from the reports, we propose a dictionary and model-dependent radiology report refinement method. Specifically, we develop an iterative vision-language representation learning framework. In the first iteration, we train a high-capacity vision-language representation learning model using the images and raw radiology reports. Then, we construct a clinical dictionary, which links keywords in raw radiology reports with medical knowledge-supplemented sentences. With the trained image and text encoders, we calculate two model-optimized knowledge-enhancement metrics to guide the report refinement process. In the second iteration, we replace the raw radiology reports with the refined versions to fine-tune the vision-language representation learning model. Importantly, we do not design specific modules to

simplify the reports. Instead, we rely on the dictionary and the model itself to identify and focus on the important information. By accessing both the raw radiology reports and the refined versions, our method avoids the loss of critical details while making full use of the reports, benefiting from the hints provided by the refined knowledge.

3. Method

The primary objective of this study is to refine the radiology reports to enhance vision-language representation learning via a novel iterative learning framework. Here, we first describe the iterative vision-language representation learning framework in Sec. 3.1. Our main contribution of knowledge refinement for radiology reports is presented in Sec. 3.2.

3.1 Iterative vision-language representation learning

Our proposed framework involves training a multi-scale contrastive learning model in two iterations. In the first iteration, the model takes images and raw radiology reports as inputs, aiming to gain a general understanding of the patient's condition. Then, the radiology reports are refined using our designed key semantic knowledge-emphasized refinement method. It is important to note that this refinement method utilizes the model trained in the first iteration. In the second iteration, the inputs to the model are changed to images and refined reports. This iteration focuses on further refining the model to capture the essential fine-grained features from the images, which are crucial for downstream analysis tasks. The details of the multi-scale contrastive learning model (Fig. 2(a)) are described in this section, while the report refinement method (Fig. 2(b)) will be elaborated in Sec. 3.2.

3.1.1 Multi-scale contrastive learning

In this section, we introduce the multi-scale contrastive learning model, a simple but effective vision-language model consisting of three components, including the image encoder E_v with the image projection block P_v , text encoder E_t with the corresponding text projection block P_t , and fusion module (Fig. 2(a)).

We employ a vision transformer as our image encoder [27], which can learn complex spatial relationships and capture long-range dependencies in the images. It extracts a number of image features corresponding to different input image patches $\tilde{r}_v = E_v(X_v) \in \mathbb{R}^{K_v \times D_v}$, where K_v indicates K_v image patches and D_v is the dimension of the extracted image features. The projection block P_v projects the features to a joint space of C dimensions, and we get the local image representations $r_v = P_v(\tilde{r}_v) \in \mathbb{R}^{K_v \times C}$. Then, average pooling is applied to r_v , which generates the global image representations $R_v \in \mathbb{R}^C$. For each radiology report, we first divide it into multiple sentences. Then, a wordpiece tokenizer is utilized to convert the processed reports into

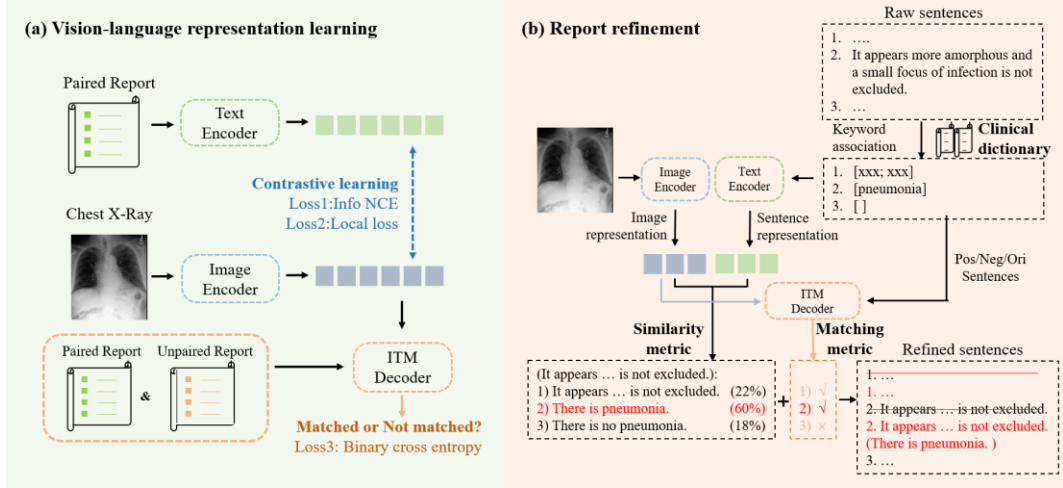


Figure 2. The two major components of our framework. (a) The vision-language representation learning model with image-text matching determination capability. (b) The key semantic knowledge-emphasized report refinement method.

a sequence of tokens that can be analyzed by the text encoder E_t . Here, we adopt BERT [28] as our E_t . It generates the corresponding sentence representations as $\tilde{r}_t = E_t(X_t) \in \mathbb{R}^{K_t \times D_t}$, where K_t indicates K_t sentences and D_t is the dimension of the extracted text features. Similarly, P_t projects \tilde{r}_t to the same joint space of C dimensions as the image branch, and the local text representations are $r_t = P_t(\tilde{r}_t) \in \mathbb{R}^{K_t \times C}$. The global text representations are generated by aggregating the local representations $R_t = \sum_{i=0}^{K_t} r_{ti} \in \mathbb{R}^C$.

A symmetric contrastive loss for the global alignment between the image and text representations is calculated:

$$L_g = -\frac{1}{N} \sum_{i=1}^N \left(\log \frac{\exp(\langle R_{vi}, R_{ti} \rangle / \tau_1)}{\sum_{j=1}^N \exp(\langle R_{vi}, R_{tj} \rangle / \tau_1)} + \log \frac{\exp(\langle R_{ti}, R_{vi} \rangle / \tau_1)}{\sum_{j=1}^N \exp(\langle R_{ti}, R_{vj} \rangle / \tau_1)} \right)$$

$\langle R_{vi}, R_{ti} \rangle$ indicates the cosine similarity between the two global features R_{vi} and R_{ti} . N is the batch size. τ_1 is a temperature parameter.

To promote the local alignment between the image and text representations, we follow the practice reported in GLoRIA [23]. Particularly, a similarity matrix (s) is obtained by computing the dot-product of the local text and image representations, $s = r_t \cdot r_v^T \in \mathbb{R}^{K_t \times K_v}$, which reflects the similarity between K_t sentences and K_v image patches. Then, it is normalized, $S_{i,j} = \frac{\exp(s_{i,j}/\tau_2)}{\sum_{k=1}^{K_v} \exp(s_{i,k}/\tau_2)}$, where τ_2 is a another temperature parameter. With S , we obtain the context-enhanced image representations to the given sentence $\widehat{r}_{vi} = \sum_{j=0}^{K_v} S_{i,j} r_{v,j}$. Finally, we aggregate the similarities between all K_t sentences and their corresponding enhanced image representations by a matching

function M , $M(X_v, X_t) = \log(\sum_{i=1}^{K_t} \exp(\langle \widehat{r}_{v_i}, r_{t_i} \rangle / \tau_3))^{\tau_3}$, where τ_3 is a temperature parameter. Similar to the global alignment, a symmetric local contrastive loss is defined as:

$$L_l = -\frac{1}{N} \sum_{i=1}^N \left(\log \frac{\exp(M(X_{vi}, X_{ti})/\tau_2)}{\sum_{j=1}^N \exp(M(X_{vi}, X_{tj})/\tau_2)} + \log \frac{\exp(M(X_{vi}, X_{ti})/\tau_2)}{\sum_{j=1}^N \exp(M(X_{vj}, X_{ti})/\tau_2)} \right)$$

3.1.2 Image-text matching determination

Image-Text Matching (ITM) is a binary classification task in which the model utilizes a language decoder with a linear layer to predict whether the input image-text pairs are positive (matching) or negative (non-matching). ITM has been proposed to capture fine-grained alignment between visual and textual information [29]. In this paper, we introduce an enhanced application for determining the correctness of sentences generated from a dictionary. We employ a BERT base decoder, as described in [30], but do not utilize the hard-sample strategy due to the frequent presence of text with similar semantics in medical reports. The application of this module will be elaborated in detail in Sec. 3.2.

We employ a straightforward binary cross-entropy loss for training the ITM module, denoted as L_{itm} . Therefore, in combination with the masked language model loss L_{mlm} utilized in E_t , the final loss used for training the multi-scale contrastive learning model is:

$$L = L_g + L_l + L_{itm} + L_{ml}$$

3.2 Key semantic knowledge-emphasized report refinement

Following the preparation outlined in Sec. 3.1, we have a pre-trained model with image-text matching determination capabilities ready to extract preliminary visual-language features. In this section, we focus on report refinement for fine-tuning the pre-trained model, as depicted in Fig. 2(b).

To facilitate report refinement, we begin by constructing a clinical dictionary. This dictionary is utilized to extract keywords from complex sentences, aiding in semantic confirmation. It links specific regions with keywords relevant to various diseases. For example, the report with keywords “heart” or “cardiac” is highly linked to the disease “cardiomegaly”. Once a medical sentence is classified as related to a particular disease type, we provide both positive and negative descriptions concerning that disease. A brief description of “cardiomegaly” could be: “There is (no) cardiomegaly”. We can also employ more specialized descriptions to improve the reliability of sentence selection, such as the positive sentence generated by GPT-4: “The cardiac silhouette is enlarged, consistent with cardiomegaly, suggesting underlying cardiac enlargement or pathology.” In the supplementary file, we provide the details table of the constructed

clinical dictionary (Supplementary Table S1). Customized statements can lead to the generation of more diverse and robust sentences.

Next, we input the image, along with all the sentences, including the original sentence and the supplemented ones, into the trained contrastive model and ITM decoder. The outputs are then utilized to assess whether the supplemented sentences accurately describe the patient's condition. We employ two metrics for this assessment: 1) A similarity metric is determined based on the pre-trained contrastive model, and 2) A matching metric is obtained using the trained ITM decoder with a binary linear classifier.

By combining these two metrics, we select the matched sentence with the highest similarity rank to supplement the original sentence. An example is illustrated in Fig. 2(b). The original sentence “It appears more amorphous and a small focus of infection is not excluded.” would be supplemented with “There is pneumonia”. Please note that although we provide professionally generated sentences from GPT-4 in the dictionary, we still employ simpler sentence patterns (e.g., “There is pneumonia”) for supplementation to enhance the model's comprehension.

Finally, we utilize the refined reports enriched with newly acquired knowledge for fine-tuning the model, directing the model's attention towards crucial information.

4. Experiments and Results

4.1 Datasets

For model training, we utilized the X-ray images and corresponding radiology reports from the MIMIC-CXR V2 dataset [31]. The model evaluation involved four tasks: fine-tuning disease classification, fine-tuning region-of-interest segmentation, zero-shot disease classification, and zero-shot phrase grounding. To perform disease classification, we incorporated four X-ray datasets, CheXpert [13], NIH ChestX-ray [12], RSNA Pneumonia [32], and SIIM-ACR Pneumothorax¹. For fine-tuning segmentation, we adopted the SIIM-ACR Pneumothorax dataset. For zero-shot phrase grounding, we utilized the MS-CXR dataset [26].

MIMIC-CXR V2 is a large dataset comprising 377,110 chest X-rays obtained from 227,827 imaging studies [31]. These studies were conducted at the Beth Israel Deaconess Medical Center between 2011 and 2016. Each image is accompanied by a corresponding free-text radiology report. In our study, we utilized all the available data from this dataset for model training.

CheXpert consists of 224,316 chest X-rays obtained from 65,240 patients. Following the official practice outlined by [13], we report the classification results for five selected pathologies, including atelectasis, cardiomegaly, consolidation, edema, and pleural

1. <https://www.kaggle.com/c/siim-acr-pneumothorax-segmentation>

effusion. Since the official test set is not publicly available, we adopted the approach from a previous study [17] and employed the official validation set as our test set. Additionally, we randomly sampled 5,000 samples from the official training set to construct our validation set, similar to [20]. For the fine-tuning evaluation, our training, validation, and testing sets contain 218,414, 5,000, and 234 images, respectively. For the zero-shot evaluation, only the 234 testing images were employed.

NIH ChestX-ray offers 112,120 chest X-rays for the classification of 14 pathologies [12]. Similarly, for fine-tuning evaluation, we divided the dataset into training, validation, and testing sets, following a split ratio of 7:2:1.

RSNA Pneumonia provides data for the binary classification task of pneumonia vs. normal. In accordance with the official configuration, the training, validation, and testing sets consist of 25,184, 1,500, and 3,000 images, respectively [32].

SIIM-ACR Pneumothorax is a dataset that consists of more than 120,000 chest X-rays, with each image being accompanied by precise manual segmentation masks of the pneumothorax regions. Following [23], we divided the dataset into three subsets: 70% for training, 15% for validation, and 15% for testing.

MS-CXR provides bounding box annotations along with paired sentences that describe the clinical findings [26]. The dataset includes a total of 1,162 annotations of 881 cases, and we utilized all of them for the evaluation.

4.2 Comparison methods

We compared our framework with various existing state-of-the-art vision-language representation learning methods to validate its effectiveness. These methods include ConVIRT [17], GLoRIA [23], BioViL [26], M³AE [21], REFERS [24], MGCA [33], CheXzero [25], MedKLIP [18], M-FLAG [22], and Med-UniC [34]. The specific contributions of most of these methods to the field have been discussed in Sec. 2. It should be noted that we did not try to re-implement these existing methods. Instead, we compared our results with the reported results in the original papers or other published papers directly.

For the evaluation of fine-tuning disease classification, we compared our method with ConVIRT, GLoRIA, BioViL, M³AE, REFERS, MedKLIP, and M-FLAG. For the evaluation of fine-tuning pneumothorax region segmentation, we compared our method with ConVIRT, GLoRIA, MGCA, M-FLAG, and Med-UniC. For the evaluation of zero-shot disease classification, we compared our method with ConVIRT, GLoRIA, BioViL, and CheXzero. For the zero-shot phrase grounding evaluation, we compared our method with ConVIRT, GLoRIA, and BioViL.

4.3 Implementation details

In our framework, we adopted the widely used ViT-B/16 as our image encoder and BERT with a width of 768 as our text encoder and ITM decoder. The mask ratio used in BERT was set to 0.15. We set the batch size to 128, with 50 epochs for initializing the model (the first iteration) and 10 for the fine-tuning process (the second iteration). We utilized the AdamW optimizer with an initial learning rate of $1.5e-4$, a weight decay of 0.05, $\beta_1=0.9$, and $\beta_2=0.95$. All experiments were implemented using PyTorch, and we used 4 NVIDIA A100 GPUs in parallel.

For the fine-tuning disease classification evaluation, we utilized the SGD optimizer with a momentum of 0.9. The best learning rate was searched in the range of $8e-3$ to $1e-4$ to achieve optimal validation performance. For the fine-tuning segmentation task, we utilized the AdamW optimizer with the learning rate of $5e-6$, $2e-5$, and $2e-5$ for 1%, 10%, and 100% labeling ratios.

4.4 Evaluation metrics

For disease classification, we evaluated the performance using the area under the curve (AUC) score. We calculated the average AUC scores for the respective datasets, as well as disease-level scores whenever possible. For region-of-interest segmentation, we employed the Dice similarity coefficient (Dice). For phrase grounding, we assessed the results based on the Intersection over Union (IoU) score and the contrast-to-noise ratio (CNR) value. IoU measures the overlap between the generated saliency maps and the ground-truth segmentation labels. CNR evaluates the contrast difference inside and outside the bounding box.

4.5 Results for fine-tuning disease classification

In this section, we present the disease classification results of different methods in fine-tuning settings. Three datasets (CheXpert, NIH ChestX-ray, and RSNA Pneumonia) were evaluated. For each dataset, we utilized three percentages of labeled data (1%, 10%, and 100%) during the fine-tuning process to investigate the influence of the fine-tuning sample number on the classification performance.

Table 1 lists the AUC scores of different methods. Overall, our proposed framework outperforms the seven comparison methods under all experimental settings, demonstrating its effectiveness for this task of fine-tuning disease classification. Additionally, consistent trends can be observed across all methods, with classification for the NIH ChestX-ray dataset being the most challenging, followed by CheXpert and RSNA Pneumonia. Apart from achieving the highest scores on all three datasets, our proposed framework exhibits more significant improvements on the most difficult

dataset, NIH ChestX-ray. For example, when utilizing 10% of the training samples, our method increases the AUC scores by 2.6%, 0.2%, and 0.6% on NIH ChestX-ray, CheXpert, and RSNA Pneumonia, respectively. This observation indicates that our proposed framework can better handle difficult samples compared to the comparison methods.

Table 1. Fine-tuning disease classification results (AUC: %), on three datasets using different ratios of labeled samples for fine-tuning. “-” indicates no results have been reported in existing literature for the corresponding experimental setting.

Methods	CheXpert			NIH ChestX-ray			RSNA Pneumonia		
	1%	10%	100%	1%	10%	100%	1%	10%	100%
ConVIRT	85.9	86.8	87.3	-	-	-	77.4	80.1	81.3
GLoRIA	86.6	87.8	88.1	-	-	-	86.1	88.0	88.6
BioVil	-	-	-	-	-	-	88.1	88.4	89.1
M ³ AE	86.2	87.3	87.9	-	-	-	89.0	90.8	92.3
REFERS	87.2	88.1	88.2	76.7	80.9	84.7	89.4	91.6	92.7
MedKLIP	-	-	-	77.2	78.9	83.2	87.3	88.0	89.3
M-FLAG	-	-	-	62.2	71.6	78.7	-	-	-
Ours	88.0	88.3	88.4	78.6	83.5	85.6	91.0	92.2	93.2

Furthermore, it is inspiring to note that the performance improvement of our proposed framework is more pronounced when employing fewer fine-tuning samples. Specifically, compared to the respective best-performing comparison methods, our proposed framework increases the AUC score by 0.8% when utilizing 1% of the training samples on CheXpert. However, this improvement decreases to 0.2% when utilizing 10% and 100% of the training samples. Similarly, our proposed framework increases the AUC scores by 1.4% and 1.6% when utilizing 1% of the training samples on NIH ChestX-ray and RSNA Pneumonia, respectively. Both values are smaller when 100% training samples are introduced. This phenomenon reflects the data efficiency of our proposed framework compared to the seven state-of-the-art methods. With the designed iterative learning process and the report refinement method, our framework can better leverage useful information from limited data for the task of disease classification.

In addition to the mean AUC scores, we also provide the classification results for the 14 chest pathologies specific to the NIH ChestX-ray dataset (Table 2). Since most existing vision-language representation learning methods lack these disease-level results (except for REFERS), we included several image self-supervised methods (Model Genesis [35], C2L [36], Context Restoration [37], and TransVW [38]), as well as an ImageNet pre-trained model [12], for comparison. Across most diseases, our proposed framework consistently achieves the highest AUC scores, thereby validating its effectiveness in fine-grained disease classification.

Table 2. Disease-level classification results (AUC: %) on the NIH ChestX-ray dataset using different ratios of labeled samples for fine-tuning.

Labeling Ratios	Methods															
		Average	Atelectasis	Cardiomegaly	Consolidation	Edema	Effusion	Emphysema	Fibrosis	Hernia	Infiltration	Mass	Nodule	Pleural Thickening	Pneumonia	Pneumothorax
1%	MedKLIP	77.2	-	-	-	-	-	-	-	-	-	-	-	-	-	-
	M-FLAG	62.2	-	-	-	-	-	-	-	-	-	-	-	-	-	-
	REFERS	76.7	77.5	85.6	78.6	84.9	85.4	79.5	72.3	77.1	67.5	76.2	66.5	71.6	69.3	81.7
	Model Genesis	70.3	72.1	67.1	75.8	76.1	80.6	72.6	64.8	73.5	65.7	65.2	62.2	67.6	64.8	76.2
	C2L	71.1	75.1	67.1	77.6	75.1	83.4	71.5	66.8	70.0	63.8	70.1	66.2	68.1	65.7	74.4
	Context Restoration	67.8	69.1	64.4	73.2	73.8	78.1	70.0	62.1	70.2	65.2	62.4	59.1	65.0	62.2	73.8
	TransVW	71.3	74.5	68.9	76.7	79.8	81.1	67.9	68.7	68.2	66.8	66.5	66.2	68.5	68.8	75.0
	ImageNet Pre-training	69.8	73.3	69.6	76.0	81.7	80.5	67.1	64.9	64.8	65.8	67.0	62.3	65.7	65.0	74.0
	Ours	78.5	77.6	89.6	78.6	87.3	86.7	86.2	68.9	84.1	66.9	81.1	68.3	69.8	69.4	84.4
	10%	MedKLIP	78.9	-	-	-	-	-	-	-	-	-	-	-	-	-
M-FLAG		71.6	-	-	-	-	-	-	-	-	-	-	-	-	-	-
REFERS		80.9	80.1	89.8	79.5	87.8	87.5	88.2	77.2	86.1	69.6	82.0	72.8	74.2	72.2	85.6
Model Genesis		76.0	77.2	72.8	77.5	85.7	85.2	81.0	75.3	78.0	68.4	73.1	69.5	72.2	67.7	80.4
C2L		76.6	78.0	75.5	77.5	84.1	85.7	81.2	73.7	79.5	67.4	77.5	71.7	72.0	67.3	81.9
Context Restoration		73.8	75.5	70.6	77.1	84.5	84.2	79.4	73.1	67.5	68.1	70.9	66.9	71.7	65.2	79.1
TransVW		74.4	76.5	70.8	77.6	83.0	84.8	79.7	69.9	74.7	68.5	72.1	68.3	72.4	63.2	79.6
ImageNet Pre-training		74.4	74.2	79.8	75.9	85.7	83.2	80.4	72.1	74.0	64.1	71.7	65.6	69.6	66.2	79.7
Ours		83.5	82.1	91.3	80.3	88.9	88.3	91.2	83.2	93.1	70.4	85.6	74.4	77.7	74.5	87.6
100%		MedKLIP	83.2	-	-	-	-	-	-	-	-	-	-	-	-	-
	M-FLAG	78.7	-	-	-	-	-	-	-	-	-	-	-	-	-	-
	REFERS	84.7	83.0	92.3	82.1	90.2	88.7	91.4	83.9	93.3	74.1	85.5	76.7	78.5	77.0	89.1
	Model Genesis	81.0	78.8	84.5	79.2	87.8	86.6	89.7	81.0	85.2	71.1	81.9	73.2	75.8	73.0	85.6
	C2L	82.2	81.1	90.2	81.0	88.1	88.0	88.3	80.8	86.8	72.0	82.7	74.1	76.2	75.3	85.9
	Context Restoration	78.7	75.8	82.9	76.4	86.6	84.8	88.2	78.6	83.0	70.0	79.6	69.5	73.2	69.4	84.0
	TransVW	81.7	79.8	85.0	80.0	88.2	87.1	90.1	81.8	85.9	72.3	82.6	74.4	76.6	74.0	86.1
	ImageNet Pre-training	80.0	78.3	89.3	77.6	87.9	85.9	87.4	78.5	88.8	65.9	79.9	70.7	74.5	71.0	84.7
	Ours	85.6	83.9	92.7	82.1	90.8	89.4	93.6	86.2	94.7	72.2	87.3	78.3	80.1	77.7	90.2

4.6 Results for fine-tuning pneumothorax region segmentation

Region-of-interest segmentation is another important medical image analysis task that offers various clinical applications, such as disease progression evaluation and treatment planning. We evaluate the effectiveness of our proposed framework by applying it to segment the pneumothorax regions using the SIIM-ACR Pneumothorax dataset in the fine-tuning setting. Results are reported in Table 3.

Table 3. Results (Dice: %) for pneumothorax region segmentation on the SIIM-ACR Pneumothorax dataset using different ratios of labeled samples for fine-tuning.

Methods	1%	10%	100%
ConVIRT	25.0	43.2	59.9
GLoRIA	35.8	46.9	63.4
MGCA	49.7	59.3	64.2
M-FLAG	52.5	61.2	64.8
Med-UniC	56.7	62.2	64.4
Ours	60.0	72.7	88.7

Similar to the fine-tuning disease classification task, three different ratios of labeled samples were employed to fine-tune the model for pneumothorax region segmentation. Significant improvements in segmentation performance across all three ratios are obtained. Notably, as more labeled samples are introduced for fine-tuning, the segmentation performance displays a more pronounced enhancement. Specifically, compared to the respective best-performing comparison methods, the Dice similarity score is increased by 3.3%, 10.5%, and 23.9% at the labeling ratio of 1%, 10%, and 100%, respectively. Interestingly, this trend differs from what we observed in the fine-tuning disease classification task, where larger improvements were observed with fewer fine-tuning samples. One possible explanation for this discrepancy is that segmentation is a more challenging task than classification, demanding more localized representations. Our proposed framework learns strong visual representations, which can be further refined when provided with additional hints from the fine-tuning samples. Consequently, these refined representations enable better discrimination of the target regions from the surrounding background. Nevertheless, it is an intriguing observation, and we plan to investigate it further in our following studies.

4.7 Results for zero-shot disease classification

In this section, we present the zero-shot disease classification results on two datasets, RSNA Pneumonia and SIIM-ACR Pneumothorax. Table 4 lists the results obtained by different methods. Among the four comparison methods, different trends are observed in the AUC scores on the two datasets. On the RSNA Pneumonia dataset, GLoRIA achieves the lowest mean AUC score, while CheXzero obtains the highest score. On the SIIM-ACR Pneumothorax dataset, although GLoRIA consistently achieves the lowest classification results, the best score is given by BioViL instead of CheXzero. This discrepancy suggests that the two datasets may possess different data characteristics that affect the learning process.

Table 4. Zero-shot disease classification results (AUC: %) on the RSNA Pneumonia and SIIM-ACR Pneumothorax datasets.

Method	RSNA	SIIM
ConVIRT	80.4	64.3
GLoRIA	71.5	53.4
BioViL	82.8	70.8
CheXzero	85.8	68.8
Ours	86.0	87.2

Compared to the four existing state-of-the-art methods, our proposed framework consistently demonstrates enhanced performance on both datasets. Particularly, on the SIIM-ACR Pneumothorax dataset, our framework achieves a remarkable 16.4% increase in AUC score when compared to the best-performing comparison method, BioViL, thereby validating the effectiveness of the proposed report refinement method

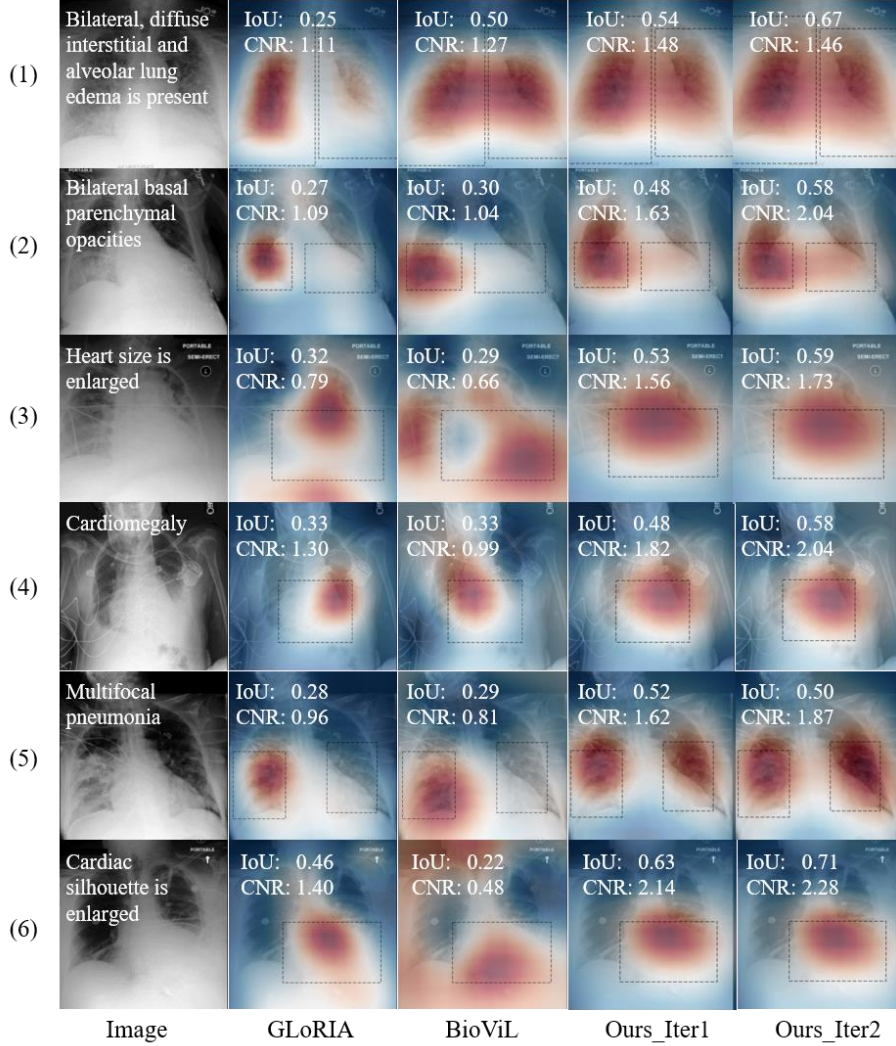


Figure 3. Visualizations of phrase grounding with free text on the MS-CXR dataset. (1) to (6) represent six examples in the dataset. White color sentences are the provided free-text annotations. Dashed boxes indicate the annotations outlined by clinical experts. “Ours_Iter1” and “Ours_Iter2” represent the models trained after the first and second iterations in our framework, respectively.

and iterative learning process.

In addition, we notice that the improvement achieved by our framework in the zero-shot setting is comparable to that in the fine-tuning setting. Referring back to Table 1, on the RSNA Pneumonia dataset, our framework increases the AUC scores by 2.9%, 3.8%, and 3.2% at 1%, 10%, and 100% labeling ratios, respectively, compared to the scores achieved by BioViL. Here, in the zero-shot setting, our framework demonstrates a 3.2% increase in AUC, from 82.8% to 86.0%. This observation further validates the data-efficient capability of the proposed framework, as it effectively enhances the performance regardless of the quantity of the provided fine-tuning samples.

4.8 Results for zero-shot phrase grounding

Phrase grounding serves as a powerful tool for improving the interpretability of deep learning models. We evaluated the zero-shot phrase grounding performance of different methods using the MS-CXR dataset (Table 5 and Fig. 3).

The quantitative results in Table 5 demonstrate that our proposed framework can effectively enhance the zero-shot phrase grounding performance of the vision-language representation learning model, as evidenced by both evaluation metrics, CNR and mIoU. Although the increase in mIoU is relatively small, the improvement in CNR is noteworthy. Specifically, our framework achieves a CNR improvement of 0.546, 0.434, and 0.337 when compared to ConVIRT, GLoRIA, and BioViL, respectively. CNR, which measures the difference between the similarity values of inner and outer bounding box regions without relying on hard threshold values, is a more objective metric that could be more clinically relevant, particularly when heatmap visualizations are needed instead of discrete segmentation [26]. In other words, our method can be very helpful in clinical applications where heatmap visualizations can provide more informative insights.

Table 5. Zero-shot phrase grounding results on the MS-CXR dataset.

Methods	CNR	mIoU
ConVIRT	0.818	0.238
GLoRIA	0.930	0.246
BioViL	1.027	0.266
Ours	1.364	0.267

Example phrase grounding visualization results are plotted in Fig. 3. These qualitative visualization results further validate the effectiveness of our proposed framework in highlighting important regions for fine-grained analysis tasks. The two comparison methods tend to highlight irrelevant regions (GLoRIA in Fig. 3 example (3); BioViL in Fig. 3 examples (3) and (6)) or overlook important regions (GLoRIA in Fig. 3 examples (1), (2), and (5); BioViL in Fig. 3 examples (2) and (5)). In contrast, our proposed framework excels at precisely locating the crucial regions for analysis tasks across all examples. Moreover, we observe that while the model trained after the first iteration in our framework can already identify the important regions, the second iteration of model fine-tuning further enhances the highlighting of these regions for subsequent analysis, which is also indicated by the increased IoU and CNR scores.

5. Conclusion and Discussion

In this study, we developed a novel iterative vision-language representation framework that incorporates a key semantic knowledge-emphasized report refinement method. The primary objective of our work was to enhance the representation learning process by

refining complex radiology reports. Extensive experiments were conducted on five external datasets, encompassing different medical image recognition tasks and evaluation settings, to investigate the effectiveness of the proposed framework. The results consistently demonstrated that our framework outperformed existing state-of-the-art methods, showcasing its superiority and robustness.

Despite the promising results, our framework still has the following limitations. Firstly, the performance of the report refinement method relies on the constructed clinical dictionary, which can eventually impact the performance of the optimized model in downstream tasks. Currently, the dictionary was constructed semi-automatically, involving traversing all the training data. Fortunately, as shown in the supplementary file (Supplementary Table S1), the dictionary is relatively simple and straightforward to construct. Nevertheless, we intend to automate the dictionary construction process in the future to further enhance the flexibility and performance of our framework. Secondly, as the two model-optimized knowledge-enhancement metrics (similarity metric and matching metric) rely on Stage 1 trained image and text encoders, our framework needs to be trained in two iterations. In future research, we will explore methods for integrating these different steps and training the framework end-to-end.

In summary, our proposed key semantic knowledge-emphasized report refinement method effectively refined the complex radiology reports to highlight crucial information. Leveraging these refined reports, our iterative vision-language representation learning framework enables effective utilization of knowledge within radiology reports and facilitates the learning of meaningful medical image representations for various downstream medical image analysis tasks, including fine-tuning disease classification, fine-tuning region-of-interest segmentation, zero-shot disease classification, and zero-shot phrase grounding. The consistent improvement in performance across different tasks highlights the potential of our framework as a valuable medical foundation model for diverse clinical applications.

Acknowledgments

This research was partly supported by the National Natural Science Foundation of China (62222118, U22A2040), Guangdong Provincial Key Laboratory of Artificial Intelligence in Medical Image Analysis and Application (2022B1212010011), and Shenzhen Science and Technology Program (JCYJ20220531100213029, RCYX20210706092104034), Key Laboratory for Magnetic Resonance and Multimodality Imaging of Guangdong Province (2023B1212060052).

References

- [1] X. Mei, H. C. Lee, K. yue Diao, M. Huang, B. Lin, C. Liu, Z. Xie, Y. Ma, P. M. Robson, M. Chung, A. Bernheim, V. Mani, C. Calcagno, K. Li, S. Li, H. Shan,

- J. Lv, T. Zhao, J. Xia, Q. Long, S. Steinberger, A. Jacobi, T. Deyer, M. Luksza, F. Liu, B. P. Little, Z. A. Fayad, and Y. Yang, "Artificial intelligence-enabled rapid diagnosis of patients with COVID-19," *Nat. Med.*, vol. 26, no. 8, pp. 1224–1228, 2020.
- [2] C. Huang, Z. Xu, Z. Shen, T. Luo, T. Li, D. Nissman, A. Nelson, Y. Golightly, M. Niethammer, and H. Zhu, "DADP: Dynamic abnormality detection and progression for longitudinal knee magnetic resonance images from the Osteoarthritis Initiative," *Med. Image Anal.*, vol. 77, p. 102343, 2022.
- [3] K. Swanson, E. Wu, A. Zhang, A. A. Alizadeh, and J. Zou, "From patterns to patients: Advances in clinical machine learning for cancer diagnosis, prognosis, and treatment," *Cell*, vol. 186, no. 8, pp. 1772–1791, 2023.
- [4] W. Huang, H. Yang, X. Liu, C. Li, I. Zhang, R. Wang, H. Zheng, and S. Wang, "A coarse-to-fine deformable transformation framework for unsupervised multi-contrast MR image registration with dual consistency constraint," *IEEE Trans. Med. Imaging*, vol. 40, no. 10, pp. 2589–2599, 2021.
- [5] W. Wang, Q. Xia, Z. Yan, Z. Hu, Y. Chen, W. Zheng, X. Wang, S. Nie, D. Metaxas, and S. Zhang, "AVDNet: Joint coronary artery and vein segmentation with topological consistency," *Med. Image Anal.*, vol. 91, p. 102999, 2024.
- [6] R. Gu, G. Wang, J. Lu, J. Zhang, W. Lei, Y. Chen, W. Liao, S. Zhang, K. Li, D. N. Metaxas, and S. Zhang, "CDDSA: Contrastive domain disentanglement and style augmentation for generalizable medical image segmentation," *Med. Image Anal.*, vol. 89, no. 2023, p. 102904, 2023.
- [7] Y. Zhou, W. Huang, P. Dong, Y. Xia, and S. Wang, "D-UNet: A dimension-fusion U shape network for chronic stroke lesion segmentation," *IEEE/ACM Trans. Comput. Biol. Bioinforma.*, vol. 18, no. 3, pp. 940–950, 2021.
- [8] S. Wang, C. Li, R. Wang, Z. Liu, M. Wang, H. Tan, Y. Wu, X. Liu, H. Sun, R. Yang, X. Liu, J. Chen, H. Zhou, I. Ben Ayed, and H. Zheng, "Annotation-efficient deep learning for automatic medical image segmentation," *Nat. Commun.*, vol. 12, p. 5915, 2021.
- [9] Z. Xu, Y. Wang, D. Lu, X. Luo, J. Yan, Y. Zheng, and R. K. Yu Tong, "Ambiguity-selective consistency regularization for mean-teacher semi-supervised medical image segmentation," *Med. Image Anal.*, vol. 88, p. 102880, 2023.
- [10] G. Wang, X. Luo, R. Gu, S. Yang, Y. Qu, S. Zhai, Q. Zhao, K. Li, and S. Zhang, "PyMIC: A deep learning toolkit for annotation-efficient medical image segmentation," *Comput. Methods Programs Biomed.*, vol. 231, p. 107398, 2023.
- [11] S. Zhang and D. Metaxas, "On the challenges and perspectives of foundation models for medical image analysis," *Med. Image Anal.*, vol. 91, no. May 2023, p. 102996, 2024.
- [12] X. Wang, Y. Peng, L. Lu, Z. Lu, M. Bagheri, and R. M. Summers, "ChestX-ray8: Hospital-scale chest X-ray database and benchmarks on weakly-supervised classification and localization of common thorax diseases," in *IEEE Conference on Computer Vision and Pattern Recognition (CVPR)*, 2017, pp. 2097–2106.
- [13] J. Irvin, P. Rajpurkar, M. Ko, Y. Yu, S. Ciurea-Ilicus, C. Chute, H. Marklund, B.

- Haghgoo, R. Ball, K. Shpanskaya, J. Seekins, D. A. Mong, S. S. Halabi, J. K. Sandberg, R. Jones, D. B. Larson, C. P. Langlotz, B. N. Patel, M. P. Lungren, and A. Y. Ng, “CheXpert: A large chest radiograph dataset with uncertainty labels and expert comparison,” *33rd AAAI Conf. Artif. Intell.*, pp. 590–597, 2019.
- [14] G. Kwon, Z. Cai, A. Ravichandran, E. Bas, R. Bhotika, and S. Soatto, “Masked vision and language modeling for multi-modal representation learning,” in *International Conference on Learning Representations (ICLR)*, 2023.
- [15] W. Wang, H. Bao, L. Dong, J. Bjorck, Z. Peng, Q. Liu, K. Aggarwal, O. K. Mohammed, S. Singhal, S. Som, and F. Wei, “Image as a foreign language: BEIT pretraining for vision and vision-language tasks,” in *IEEE Conference on Computer Vision and Pattern Recognition (CVPR)*, 2023, pp. 19175–19186.
- [16] X. Chen, X. Wang, S. Changpinyo, A. Piergiovanni, P. Padlewski, D. Salz, S. Goodman, A. Grycner, B. Mustafa, L. Beyer, A. Kolesnikov, J. Puigcerver, N. Ding, K. Rong, H. Akbari, G. Mishra, L. Xue, A. Thapliyal, J. Bradbury, W. Kuo, M. Seyedhosseini, C. Jia, B. K. Ayan, C. Riquelme, A. Steiner, A. Angelova, X. Zhai, N. Houlsby, and R. Soricut, “PaLI: A jointly-scaled multilingual language-image model,” in *International Conference on Learning Representations (ICLR)*, 2023.
- [17] Y. Zhang, H. Jiang, Y. Miura, C. D. Manning, and C. P. Langlotz, “Contrastive learning of medical visual representations from paired images and text,” in *Proceedings of Machine Learning Research*, 2022, vol. 182, pp. 1–23.
- [18] C. Wu, X. Zhang, Y. Zhang, Y. Wang, and W. Xie, “MedKLIP: Medical knowledge enhanced language-image pre-training in radiology,” in *IEEE/CVF International Conference on Computer Vision (ICCV)*, 2023, pp. 21372–21383.
- [19] X. Zhang, C. Wu, Y. Zhang, W. Xie, and Y. Wang, “Knowledge-enhanced visual-language pre-training on chest radiology images,” *Nat. Commun.*, vol. 14, no. 1, p. 4542, 2023.
- [20] H.-Y. Zhou, C. Lian, L. Wang, and Y. Yu, “Advancing radiograph representation learning with masked record modeling,” in *International Conference on Learning Representations (ICLR)*, 2023.
- [21] Z. Chen, Y. Du, J. Hu, Y. Liu, G. Li, X. Wan, and T. Chang, “Multi-modal masked autoencoders for medical vision-and-language pre-training,” in *International Conference on Medical Image Computing and Computer-Assisted Intervention (MICCAI)*, 2022, pp. 679–689.
- [22] C. Liu, S. Cheng, C. Chen, M. Qiao, W. Zhang, A. Shah, W. Bai, and R. Arcucci, “M-FLAG: Medical vision-language pre-training with frozen language models and latent space geometry optimization,” in *International Conference on Medical Image Computing and Computer-Assisted Intervention (MICCAI)*, 2023, vol. 14220 LNCS, pp. 637–647.
- [23] S. C. Huang, L. Shen, M. P. Lungren, and S. Yeung, “GLoRIA: A multimodal global-local representation learning framework for label-efficient medical image recognition,” in *Proceedings of the IEEE International Conference on Computer Vision (ICCV)*, 2021, pp. 3922–3931.
- [24] H.-Y. Zhou, X. Chen, Y. Zhang, R. Luo, L. Wang, and Y. Yu, “Generalized

- radiograph representation learning via cross-supervision between images and free-text radiology reports,” *Nat. Mach. Intell.*, vol. 4, no. 1, pp. 32–40, 2022.
- [25] E. Tiu, E. Talius, P. Patel, C. P. Langlotz, A. Y. Ng, and P. Rajpurkar, “Expert-level detection of pathologies from unannotated chest X-ray images via self-supervised learning,” *Nat. Biomed. Eng.*, vol. 6, no. 12, pp. 1399–1406, 2022.
- [26] B. Boecking, N. Usuyama, S. Bannur, D. C. Castro, A. Schwaighofer, S. Hyland, M. Wetscherek, T. Naumann, A. Nori, J. Alvarez-Valle, H. Poon, and O. Oktay, “Making the most of text semantics to improve biomedical vision-language processing,” in *European Conference on Computer Vision (ECCV)*, 2022, pp. 1–21.
- [27] A. Dosovitskiy, L. Beyer, A. Kolesnikov, D. Weissenborn, X. Zhai, T. Unterthiner, M. Dehghani, M. Minderer, G. Hiegold, S. Gelly, J. Uszkoreit, and N. Houlsby, “An image is worth 16x16 words: Transformers for image recognition at scale,” in *International Conference on Learning Representations (ICLR)*, 2021.
- [28] J. Devlin, M.-W. Chang, K. Lee, K. T. Google, and A. I. Language, “BERT: Pre-training of deep bidirectional transformers for language understanding,” in *NAAC-HIT*, 2019, pp. 4171–4186.
- [29] J. Li, R. R. Selvaraju, A. D. Gotmare, S. Joty, C. Xiong, and S. C. H. Hoi, “Align before fuse: Vision and language representation learning with momentum distillation,” in *Advances in Neural Information Processing Systems (NeurIPS)*, 2021.
- [30] J. Li, D. Li, C. Xiong, and S. Hoi, “BLIP: Bootstrapping Language-image pre-training for unified vision-language understanding and generation,” in *Proceedings of Machine Learning Research*, 2022, vol. 162, pp. 12888–12900.
- [31] A. E. W. Johnson, T. J. Pollard, N. R. Greenbaum, M. P. Lungren, C. Deng, Y. Peng, Z. Lu, R. G. Mark, S. J. Berkowitz, and S. Horng, “MIMIC-CXR-JPG, a large publicly available database of labeled chest radiographs,” vol. 14, pp. 1–7, 2019.
- [32] G. Shih, C. C. Wu, S. S. Halabi, M. D. Kohli, L. M. Prevedello, T. S. Cook, A. Sharma, J. K. Amorosa, V. Arteaga, M. Galperin-Aizenberg, R. R. Gill, M. C. B. Godoy, S. Hobbs, J. Jeudy, A. Laroia, P. N. Shah, D. Vummidi, K. Yaddanapudi, and A. Stein, “Augmenting the national institutes of health chest radiograph dataset with expert annotations of possible pneumonia,” *Radiol. Artif. Intell.*, vol. 1, no. 1, 2019.
- [33] F. Wang, Y. Zhou, S. Wang, V. Vardhanabhuti, and L. Yu, “Multi-granularity cross-modal alignment for generalized medical visual representation learning,” in *Advances in Neural Information Processing Systems (NeurIPS)*, 2022.
- [34] Z. Wan, C. Liu, M. Zhang, J. Fu, B. Wang, S. Cheng, L. Ma, C. Quilodran-Casas, and R. Arcucci, “Med-UniC: Unifying cross-lingual medical vision-language pre-training by diminishing bias,” in *Advances in Neural Information Processing Systems (NeurIPS)*, 2023.
- [35] Z. Zhou, V. Sodha, J. Pang, M. B. Gotway, and J. Liang, “Models Genesis,” *Med. Image Anal.*, vol. 67, p. 101840, 2021.

- [36] H.-Y. Zhou, S. Yu, C. Bian, Y. Hu, K. Ma, and Y. Zheng, “Comparing to learn: Surpassing imagenet pretraining on radiographs by comparing image representations,” in *International Conference on Medical Image Computing and Computer-Assisted Intervention (MICCAI)*, 2020, vol. 12261 LNCS, pp. 398–407.
- [37] L. Chen, P. Bentley, K. Mori, K. Misawa, M. Fujiwara, and D. Rueckert, “Self-supervised learning for medical image analysis using image context restoration,” *Med. Image Anal.*, vol. 58, p. 101539, 2019.
- [38] F. Haghghi, M. R. H. Taher, Z. Zhou, M. B. Gotway, and J. Liang, “Transferable visual words: Exploiting the Ssemantics of anatomical patterns for self-supervised learning,” *IEEE Trans. Med. Imaging*, vol. 40, no. 10, pp. 2857–2868, 2021.